ISSN 2079-1704. Хімія, фізика та технологія поверхні. 2025. Т. 16. № 1. С. 115-129

UDC 544.1 + 542.8 + 544.7 doi: 10.15407/hftp16.01.115

O.D. Shchehlov [1], A.P. Kusyak [1], O.I. Oranska [1], R.M. Kravchuk [2], A.L. Petranovska [1], Ya.M. Shuba [3], P.P. Gorbyk [1]

NANOSIZED LUMINESCENT HYDROXYAPATITE DOPED WITH TERBIUM: SYNTHESIS AND CHARACTERIZATION

[1] Chuiko Institute of Surface Chemistry of National Academy of Sciences of Ukraine
17 General Naumov Str., Kyiv, 03164, Ukraine, E–mail: ol.shchehlov@gmail.com
[2] Institute of Physics of National Academy of Sciences of Ukraine
46 Nauky Avenue, Kyiv, 03028, Ukraine
[3] Bogomoletz Institute of Physiology of National Academy of Sciences of Ukraine
4 Bogomoletz Str., Kyiv, 01601, Ukraine

The aim of this work is to synthesize a new nanostructured biocompatible material with a high ability to X-ray-induced luminescence. Terbium-doped hydroxyapatite known for its biocompatibility and non-toxicity was synthesized in two ways: 1) by precipitation of Ca^{2+} and Tb^{3+} ions with $(NH_4)_2HPO_4$ solution in the presence of various biocompatible modifiers (CTAB, PEG-2000, trisodium citrate dihydrate); 2) by cationic substitution of hydroxyapatite in the presence of the same modifiers at pH 4 and pH 6. The stoichiometric ratio (Ca+Tb)/P in the initial solutions was maintained at the level of biological hydroxyapatite.

Based on the results of DLS, ELS, and X-ray-induced luminescence studies, it was found that the sample with the best key properties, such as ζ-potential and X-ray-induced luminescence, was the sample of hydroxyapatite doped with 5% (mol), synthesized by co-precipitation procedure in presence of trisodium citrate dihydrate. Further studies by TEM, FTIR, FT-NIR, TG/DTG/DTA, XRD, low-temperature nitrogen adsorption-desorption, and ICP-AES confirm that the sample has a surface functionalized with citrate groups, which causes high colloidal stability and can provide high adsorption potential. The value of the (Ca+Tb)/P ratio is 2.21 (wt %), which is close to that of biological hydroxyapatite. The nanocomposite is characterized by high X-ray-induced luminescence and may be promising for adsorption immobilization of biologically active compounds.

The results of the study indicate that the optimized conditions for the synthesis of nanophosphors have been found, which are potential candidates for biomedical applications, given their luminescent properties, low toxicity, and the possibility of further surface functionalization for adsorption saturation with molecules of medical interest.

***Keywords**: nanoparticles, nanocomposites, luminescence, lanthanides, hydroxyapatite, terbium*

INTRODUCTION

The use of nanomaterials with good luminescent properties is one of the many innovative strategies for creating new systems for nanomedical applications such as drug delivery, biovisualization, photopharmacology, photo-dynamic therapy, *etc*. [1–4]. One of the most promising ways to impart luminescent properties to nanomaterials is the doping them with ions of rare earth elements (mainly lanthanides). This area of research continues to be actively developed [5–8]. Lanthanide ions are well-known for their photoluminescent properties in the visible and near-infrared regions, so luminescent nanoparticles and nanomaterials are used to visualize tissues and intracellular structures.

However, to expand their application in living cells, it is crucial to develop new biocompatible nanomaterials. A specific requirement for such nanomaterials, in addition to luminescence and magnetoresistance observable with confocal microscopes or magnetic resonance imaging (MRI), is low level of toxicity [9–10].

Clear criteria exist for the material used in doping. It must be nanoscale, biocompatible, biodegradable, and have a highly controlled synthesis pathway. Hydroxyapatite [$Ca_{10}(PO_4)_6(OH)_2$, HA] is just such a material. Moreover, it is the well-studied and widely used material in research [11–15]. Hydroxyapatite doped with rare earth elements for biological applications has been extensively studied and remains an active area of investigation.

Therefore, lanthanide-doped hydroxyapatite nanoparticles are currently under study not only as a new category of luminescent optical tags, but also as a promising alternative to organic fluorophores and quantum dots. This is especially notable due to their high quantum yield,

significant stoichiometric shift, low toxicity, high thermal and chemical stability, and sharp emission bands [16–20].

Synthetic apatite differs significantly from biological hydroxyapatite in terms of stoichiometry, composition, crystallinity, lattice parameters, thermal stability, biological activity, and resorption rate, all influenced by ionic substitution of Ca^{2+}, PO_4^{3-}, or OH^- ions. It is well-known that replacing a small amount of Ca^{2+} ions in hydroxyapatite structure alters the crystal lattice, reduces particle size, decreases crystallinity, and promotes bioresorption, which accelerates the leaching of Ca^{2+} ions into the environment. Thus, several important research challenges remain regarding achieving optimal biocompatibility and bioresorption of medical nanoparticles that have yet to be resolved [21–28].

The ionic radii of trivalent ions of stable elements from La^{3+} to Lu^{3+} are very close to that of Ca^{2+}, ranging slightly larger to slightly smaller. Previous studies have demonstrated the examples of Ca^{2+} substitution by trivalent lanthanide ions, with investigations into the physicochemical properties of these nanoparticles [30–33]. Additionally, there is an assumption that Tb-doped HA can exhibit luminescence under X-ray exposure [34–35].

This paper details the synthesis, methodology, and results of studies of synthesized samples of Tb-doped HA with a functionalized surface, focusing on X-ray-induced luminescence, size distribution, ζ-potential, chemical composition, crystal structure, porosity, and morphology.

The obtained results show that the synthesized material possesses highly favorable properties, enabling its application in the development of drug delivery systems where a photosensitive substance immobilized on the surface can be activated by X-rays to release drugs. This material, meeting the set objectives, has potential for further investigation into its adsorption capabilities for X-ray sensitive complexes, facilitating the controlled release of biologically active substances under X-ray irradiation.

EXPERIMENTAL PART

Materials. The synthesis was carried out using calcium nitrate tetrahydrate ($Ca(NO_3)_2 \cdot 4H_2O$), ammonium phosphate dibasic ($(NH_4)_2HPO_4$), terrbium (III) nitrate pentahydrate ($Tb(NO_3)_3 \cdot 5H_2O$), 25 % ammonia solution (NH_4OH), cetyltrimethylammonium bromide (CTAB) ($C_{19}H_{42}BrN$), polyethylene glycol 2000 (PEG-2000) ($H(OCH_2CH_2)_nOH$, M. w. 2000), trisodium citrate dihydrate (Na_3Citr) ($C_6H_5Na_3O_7 \cdot 2H_2O$), 65 % nitric acid solution (HNO_3), ammonium acetate ($NH_4CH_3CO_2$), acetic acid (CH_3COOH). All the used reagents are qualified as “chemically pure”. Distilled water was used as a solvent.

Preparation of terbium-doped hydroxyapatite. Hydroxyapatite (HA) matrices were synthesized by the precipitation method. According to the standard procedure, the synthesis was carried out at a temperature of 80 °C. The $Ca(NO_3)_2$ solution with adjusted pH by adding 25 % NH_4OH to pH 11 was added dropwise to an aqueous solution of $(NH_4)_2HPO_4$ under constant stirring. The molar ratio of Ca/P ions in the initial solutions was maintained at 1.67. A finely dispersed suspension of HA nanoparticles was formed in the mixed solution. The HA suspension was incubated for 1 h, collected by centrifugation (8.000 rpm), and then washed with deionized water until reaching a neutral pH.

Two ways of doping hydroxyapatite nanocrystals with terbium were chosen. The first way is the co-precipitation of Ca^{2+} and Tb^{3+} ions with $(NH_4)_2HPO_4$ solution [36–38]. The synthesis was carried out according to a procedure similar to the previously described procedure for the synthesis of HA, except that the initial solution contained $Tb(NO_3)_3$ in addition to $Ca(NO_3)_2$. The molar ratio of the (Ca+Tb)/P ions in the initial solutions was maintained at 1.67. Thus, a sample of terbium-doped hydroxyapatite (HA:Tb) was synthesized.

To obtain HA:Tb samples with a functionalized surface, substances capable of modifying the surface were added to the initial $(NH_4)_2HPO_4$ solution. The approaches proposed in previous studies [17, 30, 39–42] were used to select surface modifiers. The syntheses were performed separately in the presence of the following substances: CTAB (Ca/CTAB molar ratio is 10 : 1), PEG-2000 (15 % wt %), and Na_3Citr (Citr/Ca molar ratio is 2 : 1). The synthesis procedure was similar to the previously described HA:Tb synthesis procedure. Thus, the following samples were synthesized: pHA:Tb/CTAB, pHA:Tb/PEG and pHA:Tb/Citr (p – precipitation).

The second way of doping HA was cationic substitution of Ca^{2+} ions in the structure of HA nanoparticles with Tb^{3+} ions in buffer solutions with different pH. When choosing the conditions for doping, we used the approaches proposed in previous studies [17, 30, 32, 42–45]. The doping procedure included transferring the previously obtained HA suspension together with modifiers to acetate buffer solutions with pH 6 and pH 4, and then adding a solution of $Tb(NO_3)_3$. The modifiers were taken in the same concentrations as in the previously described procedure. The molar fraction of Tb^{3+} ions in the mixed solutions was 5 % relative to Ca^{2+} ions. The resulting mixtures were incubated for 24 hours. The samples were collected by centrifugation (8.000 rpm) and then washed with deionized water to remove excess modifiers and buffer solutions. In this way, samples for both buffer solutions were synthesized: sHA:Tb/CTAB, sHA:Tb/PEG, and sHA:Tb/Citr (s – substitution).

Characterization of terbium-doped hydroxyapatite. The obtained samples were characterized by measuring X-ray-induced luminescence spectra, following the method described in [46–48]. This was conducted using an Ocean Optics USB2000 spectrometer and OmniDriverCSharpDemo software, with the parameters set as follows: integration time of 10 seconds and averaging over 30 measurements. Spectra were obtained through an FC-UV-400-2 optical fiber connected to a diffractometer with a collimator nozzle, positioned at approximately 30 mm from the particles. Analysis of the luminescence spectra involved fitting specific regions of the spectra to the measured peaks using Gaussian curves.

The size distributions and ζ-potential of the obtained samples were measured using a Zetasizer Nano ZSP (Malvern Instruments, UK), employing Dynamic Light Scattering (DLS) and Electrophoretic Light Scattering (ELS) methods. The samples, pretreated with ultrasound (2 times for 15 minutes), were prepared at the concentration of C = 0.5 mg/ml in a solution of 0.15 M NaCl at T = 298 K. For DLS measurements, the samples were transferred to a 10 mm cuvette, while an electrophoretic cuvette was used for ELS measurements. The instrument utilized a laser with a wavelength of 632.8 nm and a scattering angle of 173°. Refractive index of 1.332 and viscosity of 0.908 mPa s were employed in the calculations.

The morphology and size of the obtained nanoparticles were investigated using JEOL 1200 EX transmission electron microscopy (JEOL, Japan). The samples were diluted in deionized water, deposited onto carbon-coated copper grids (EM Resolutions Ltd.), and air-dried at room temperature for 12 hours.

For elemental composition analysis, an ICPE-9000 (Shimadzu, Japan) equipped with inductively coupled plasma atomic emission spectroscopy (ICP-AES) was utilized. The instrument was calibrated using standard solutions of the elements of interest. Samples were prepared by dissolving 10 mg of powder in 50 ml of dilute HNO_3, followed by diluting 0.15 ml of the resulting solution in 10 ml of dilute HNO_3 for analysis.

A Nicolet iS50 IR spectrometer (Thermo Scientific, USA) was used to obtain IR spectra in the range of 4000–400 cm^{-1} using the attenuated total reflectance (ATR) mode, with a resolution of 2 cm^{-1}. Additionally, near-infrared (NIR) spectra were recorded on the same device using a special attachment for NIR measurements, covering the range of 4000–10000 cm^{-1}.

X-ray diffraction (XRD) analyses were conducted using a DRON-UM1 instrument equipped with a CuK_α filter and Bragg-Brentano focusing. The measurements were performed in the 2θ range of 5–60° with a step size of 0.05° and an exposure time of 1 second.

Thermal decomposition characteristics of the samples were investigated using the TG/DTG/DTA method on a Paulik-Paulik-Erdey derivatograph (MOM, Hungary). Measurements were carried out in a temperature range from 27 to 1000 °C at a heating rate of 10°/min under a synthetic air atmosphere (30 mL/min), using Al_2O_3 crucibles.

The BET (Brunauer-Emmett-Teller) surface area was determined via low-temperature nitrogen adsorption-desorption at -196 °C, employing a NOVA 1200e Surface Area & Pore Size Analyzer (Quantachrome, USA). The specific surface area (S_{BET}) was calculated from physical nitrogen adsorption-desorption isotherms using the BET method over a range of relative pressures (P/P_0 = 0.05–1.00). The pore size distribution (PSD) was analyzed using the BJH (Barrett-Joyner-Halenda) method. As part of the study, a sample of undoped HA (HA/Citr) was additionally synthesized in the presence of Na_3Citr for comparative purposes.

RESULTS AND DISCUSSION

Study of X-ray-induced luminescence. The luminescence spectra of the powders are shown in Fig. 1. The X-ray-induced luminescence spectra of the obtained nanoparticle samples reveal four peaks at wavelengths of 490, 545, 585, and 630 nm corresponding to the $^5D_4$-$^7F_6$, $^5D_4$-$^7F_5$, $^5D_4$-$^7F_4$, and $^5D_4$-$^7F_3$ Tb transitions, respectively. The main peak is observed at 546 nm, attributed to the $^5D_4$-$^7F_5$ Tb transitions [49]. Among the samples doped by substitution at pH 4, sHA:Tb/Citr showed the highest intensity (Fig. 1 *a*). Among the samples doped by substitution at pH 6, sHA:Tb/CTAB exhibited the highest intensity (Fig. 1 *b*). Among the samples synthesized by co-precipitation in the presence of modifiers, pHA:Tb/Citr showed the highest intensity (Fig. 1 *c*). The pHA:Tb/Citr sample exhibits higher intensity compared to all other samples (Fig. 1 *d*).

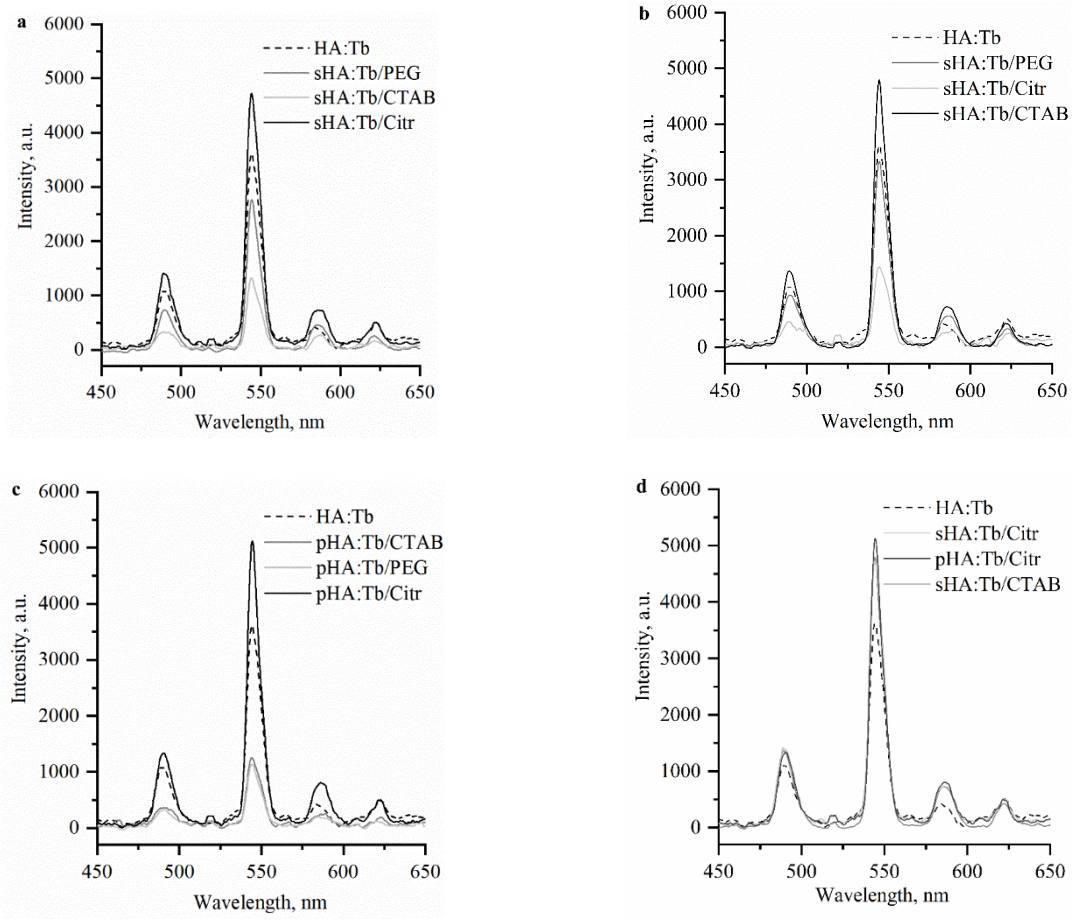

Fig. 1. X-ray-induced luminescence spectra of Tb-doped HA: *a* – by ionic substitution in the presence of modifiers at pH 4; *b* – by ionic substitution in the presence of modifiers at pH 6; *c* – by co-precipitation in the presence of modifiers; *d* – compared samples showing the best result from each synthesis route

Dynamic and electrophoretic light scattering (DLS, ELS) studies. The data obtained in this work (Table 1) indicate that unmodified HA:Tb has lower ζ-potential than HA, which correlates with an increase in the average hydrodynamic size.

Among the samples synthesized in the presence of modifiers and doped by cationic substitution at pH 4, sHA:Tb/Citr exhibits the most negative ζ-potential (-10.8 mV), so the colloidal dispersion that this sample forms in 0.9 % NaCl can be classified as relatively stable [50]. All samples synthesized in the presence of modifiers and doped at pH 6 have ζ-potential values very close to 0 (Table 2), so they form very unstable colloidal dispersions in 0.9 % NaCl.

The data also indicate that the pHA:Tb/Citr sample obtained by the co-precipitation method

has the highest ζ-potential value (-33.9 mV) compared to all other samples (Table 3). This sample forms a highly stable colloidal suspension in 0.9 % NaCl [50]. In addition to colloidal stability, a high ζ-potential may indicate higher biocompatibility of nanoparticles [51–53].

Table 1. DLS and ELS analysis of HA, HA:Tb samples, and doped by cationic substitution at pH 4 sHA:Tb/CTAB, sHA:Tb/PEG, sHA:Tb/Citr samples

Sample	Mean hydrodynamic diameter, nm	ζ-potential, mV
HA	110	-3.4
HA:Tb	141	-2.2
sHA:Tb/CTAB	186	-1.8
sHA:Tb/PEG	111	-0.3
sHA:Tb/Citr	126	-10.8

Table 2. DLS and ELS analysis of HA, HA:Tb samples, and doped by cationic substitution at pH 6 sHA:Tb/CTAB, sHA:Tb/PEG, sHA:Tb/Citr samples

Sample	Mean hydrodynamic diameter, nm	ζ-potential, mV
HA	110	-3.4
HA:Tb	141	-2.2
sHA:Tb/CTAB	233	2.4
sHA:Tb/PEG	604	1.2
sHA:Tb/Citr	205	-6.5

Table 3. DLS and ELS analysis of HA, HA:Tb, pHA:Tb/CTAB, pHA:Tb/PEG, and pHA:Tb/Citr samples

Sample	Mean hydrodynamic diameter, nm	ζ-potential, mV
HA	110	-3.4
HA:Tb	141	-2.2
pHA:Tb/CTAB	192	-5.1
pHA:Tb/PEG	226	-7.0
pHA:Tb/Citr	344	-33.9

Transmission electron microscopy. Fig. 2 shows TEM images of the synthesized HA:Tb (Fig. 2 *a*) and pHA:Tb/Citr (Fig. 2 *c*) nanoparticles as well as their size distribution according to TEM data: HA:Tb (Fig. 2 *b*) and pHA:Tb/Citr (Fig. 2 *d*). It is characteristic that the distribution of nanoparticles was relatively homogeneous. The nanoparticles are rod-shaped, which is typical for HA nanoparticles, so it can be argued that Tb-doping does not affect the morphology of nanoparticles [54–55].

The pHA:Tb/Citr sample is characterized by a change in morphology to a needle-like structure and an increase in the length of nanoparticles (length to width ratio of 1 : 10). This can explain the rather high value of the average hydrodynamic size obtained in DLS studies.

In general, the results of the size distribution obtained by TEM correlate satisfactorily with the results of DLS studies.

Elemental analysis. The results of elemental analysis performed by the ICP-AES method (Table 4) show the content of Ca, P, and Tb (wt. %) and the main indicators of compliance of biological hydroxyapatite with the stoichiometric ratios Ca/P and (Ca+Tb)/P. The synthesized sample of undoped HA was compared with the stoichiometric value of natural HA of 2.15 (wt %). The ratio of 2.60 is higher than expected and indicates P (phosphorus) deficiency of 3.44 %. This difference can be explained by the inclusion of carbonate groups from atmospheric carbon dioxide, which replace phosphate groups in the hydroxyapatite matrix [56].

For the hydroxyapatite sample doped with terbium, the calculated ratio was 2.55, and the phosphorus deficiency decreased to 3.21 %. This can be explained by the substitution of divalent calcium with trivalent terbium, which has close ionic radii. This also explains the higher (Ca+Tb)/P ratio of 2.92, reflecting the significant

difference in atomic weights between calcium and terbium. The presence of carbonate ions in the structure of the synthesized samples can positively impact their biocompatibility [57].

In the case of pHA:Tb/Citr sample, there is no phosphorus deficiency, and the (Ca+Tb)/P ratio is the closest to the natural one and is 2.21. This may be due to the fact that Na_3Citr inhibits the reaction of carbonate ions with calcium cations [58].

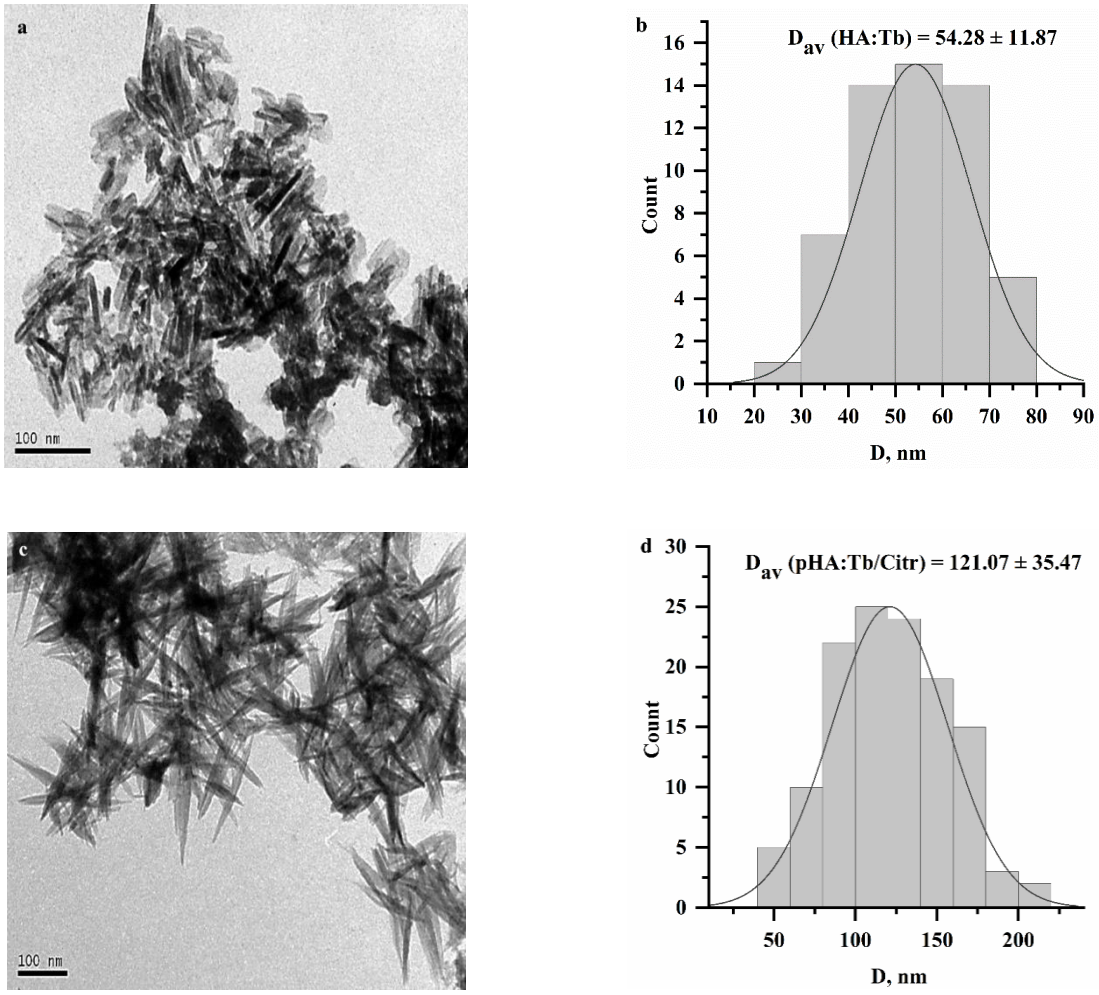

Fig. 2. TEM images of the HA:Tb (*a*) and pHA:Tb/Citr (*c*) samples and their size distribution according to TEM data: HA:Tb (*b*) and pHA:Tb/Citr (*d*)

Table 4. ICP-AES analysis of HA, HA:Tb, and pHA:Tb/Citr samples

Sample	Ca, wt. %	P, wt. %	Tb, wt. %	(Ca+Tb)/P, wt. %/wt. %	Ca/P, wt. %/wt. %
HA	43.52	16.74			2.60
HA:Tb	44.59	17.47	6.35	2.92	2.55
pHA:Tb/Citr	33.74	18.08	6.15	2.21	1.87

FTIR and FT-NIR analysis. Fig. 3 *a* shows the infrared spectra of HA, HA:Tb, and pHA:Tb/Citr. The analysis of the spectra reveals that the bands at 3570 and 630 cm^{-1} correspond to stretching vibrations and vibrations of -OH groups in HA. The presence of PO_4^{3-} groups is indicated by bands at 1088, 1020, 960, 600, 560, and 472 cm^{-1}. The band at 876 cm^{-1} is attributed to the valence vibrations of CO_3^{2-} induced by the substitution of PO_4^{3-}. The bands at 1580 and

1420 cm^{-1} represent asymmetric and symmetric valence vibrations of COO^- carboxyl groups from surface citrate groups [54, 59]. For HA and HA:Tb, the peak at 3693 cm^{-1} corresponds to OH^- stretching (Fig. 3 *b*).

The FT-NIR spectra (Fig. 4) of all three samples exhibit a broad intense band at 5180 cm^{-1} attributed to surface-adsorbed water molecules that actively form hydrogen bonds. The pHA:Tb/Citr sample shows the most intense signal indicating the highest surface activity among the studied samples. The peaks at 5320 and 7250 cm^{-1} is suggested to belong to structural water molecules with limited involvement in hydrogen bonding that is prominently visible in HA and HA:Tb samples but less in pHA:Tb/Citr. The bands at 4650 and 6950 cm^{-1} correspond to -OH structural groups that are prominently visible in HA and HA:Tb spectra and almost absent in pHA:Tb/Citr suggesting the deprotonated state of carboxyl groups.

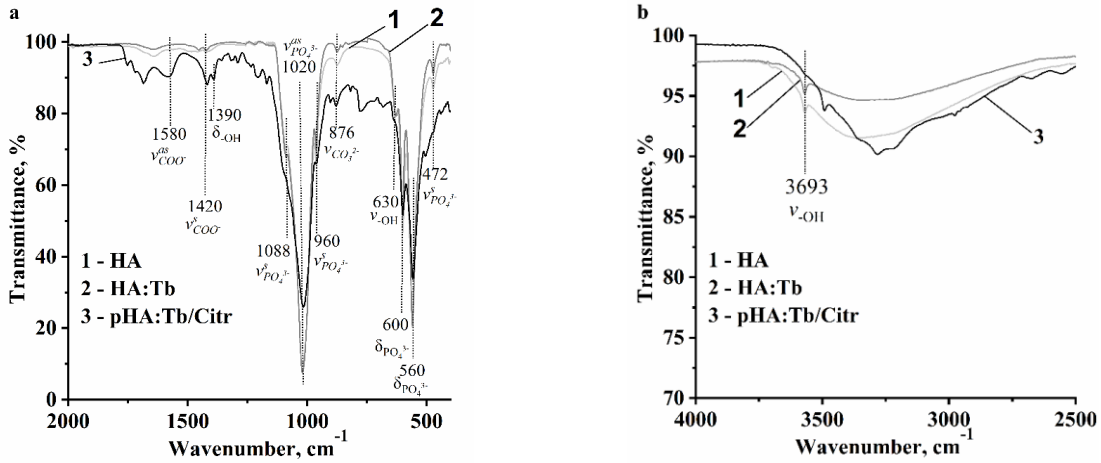

Fig. 3. Infrared spectra of HA (*1*), HA:Tb (*2*) and pHA:Tb/Citr (*3*) samples: *a* – in the range of 400–2000 cm^{-1}; *b* – in the range of 2500–4000 cm^{-1}

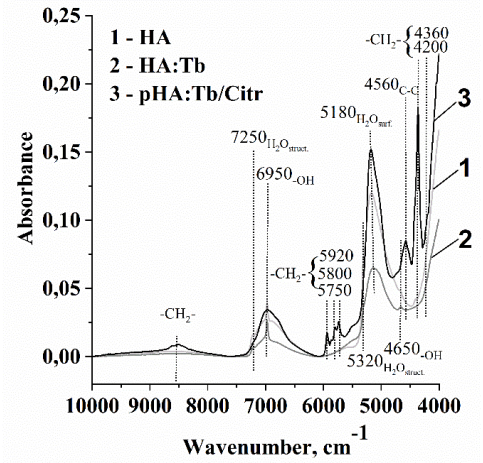

Fig. 4. FT-NIR spectra of HA (*1*), HA:Tb (*2*), and pHA:Tb/Citr (*3*) samples

The wide low-intensity band spanning 8000–9000 cm^{-1}, along with peaks at 5920, 5800, and 5750 cm^{-1}, and peaks at 4360 and 4200 cm^{-1}, correspond to structural bonds of citrate molecules (-CH_2-) and C-C bonds, respectively [60–61].

X-ray structural analysis. The X-ray diffraction (XRD) patterns of the synthesized HA, HA:Tb, and pHA:Tb/Citr materials are depicted in Fig. 5. All diffraction peaks closely match those in the ICDD database for hydroxyapatite

(PDF No. : 89-4405) confirming a hexagonal structure with space group P63/m.

The incorporation of Tb^{3+} and surface functionalization with carboxyl groups using Na_3Citr did not alter the crystal phases of the products, which remained single-phase without detecting any impurity peaks. Key peaks observed for HA, HA:Tb, and pHA:Tb/Citr samples occur at 2θ values of 25.9°, 31.8°, 34.1°, 39.9°, 46.7°, and 49.5°. These peaks correspond to crystal planes (002), (211), (112), (202), (310), (222), and (213), respectively. The size of HA crystallites, calculated using the Scherer formula, is 20 nm.

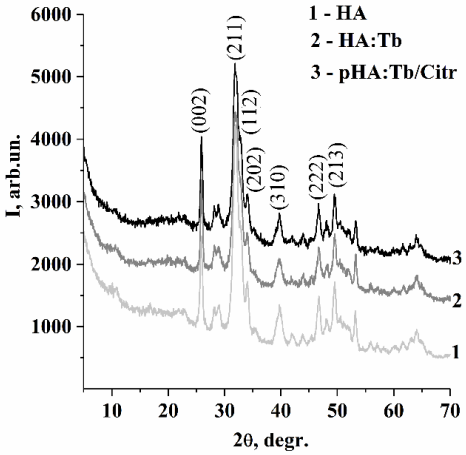

Fig. 5. XRD diffractograms of HA (*1*), HA:Tb (*2*), and pHA:Tb/Citr (*3*) samples

Differential thermal and thermogravimetric analysis. The thermogravimetric analysis (TGA) results for the HA sample between 25 and 1000 °C showed a weight loss of 6.9 % (Table 5). In contrast, pHA:Tb/Citr exhibited a higher weight loss of 12.2 % primarily attributed to slightly elevated water content (3.84 % compared to 2.76 % for HA) in the hydrate layer surrounding the precipitated pHA:Tb/Citr particles. The notably smaller average agglomerate sizes observed in TEM micrographs for pHA:Tb/Citr suggest a potentially larger surface area facilitating increased adsorption of surface water in this sample.

Corresponding differential thermal analysis (DTA) data revealed an endothermic reaction for all samples, characterized by a peak around 120 °C for HA (Fig. 6 *a*) and 125 °C for pHA:Tb/Citr (Fig. 6 *b*). The HA samples exhibited 2.83 % mass loss between 200 and 600 °C that can be due to gradual loss of lattice water. Mass loss above 600 °C can be attributed to structural dehydroxylation of HA, accompanied by an endothermic peak observed at approximately 725 °C (Fig. 6 *a*).

For the pHA:Tb/Citr sample, successive mass loss peaks were recorded in the temperature range of 290 to 420 °C (Fig. 6 *b*), with losses of 4.39 and 2.75 %, respectively. These peaks correspond to the thermal decomposition of citrate on the particle surface [62, 63].

BET surface area analysis. Low-temperature nitrogen adsorption/desorption isotherms of nanodispersed HA (*a*), HA/Citr (*b*), HA:Tb (*c*), and HA:Tb/Citr (*d*) are illustrated in Fig. 7. The results from Table 6 highlight significant differences in the textural characteristics of the synthesized samples.

The specific surface area (S_{BET}) of the HA sample was measured at 104.8 m^2/g, slightly decreasing to 94.4 m^2/g for HA/Citr. In contrast, HA:Tb exhibited a higher S_{BET} of 149.2 m^2/g, and pHA:Tb/Citr showed a value of 140.7 m^2/g indicating an almost 50 % increase in specific area due to the addition of terbium with minimal influence from citrate ions. The reason for this may be the observed increase in the porosity of the doped samples, namely, an increase in the pore volume (including the volume of micropores) and a decrease in the pore size. As shown in Fig. 7, all samples displayed a type IV isotherm that is characteristic for mesoporous materials with micropores [64, 65].

The HA sample exhibited an H1 hysteresis loop (Fig. 7 *a)*, indicating the presence of micro-, meso-, and macropores, likely representing inter-

particle spaces. The total pore volume measured was 0.48 cm^3/g with an average pore diameter of 184.5 nm.

Notably, HA synthesized in the presence of sodium citrate (HA/Citr) (Fig. 7 *b*) showed an increase in total pore volume to 0.53 cm^3/g with an average pore diameter of 225.2 nm, suggesting an enhancement in mesoporosity due to the presence of citrate ions [66].

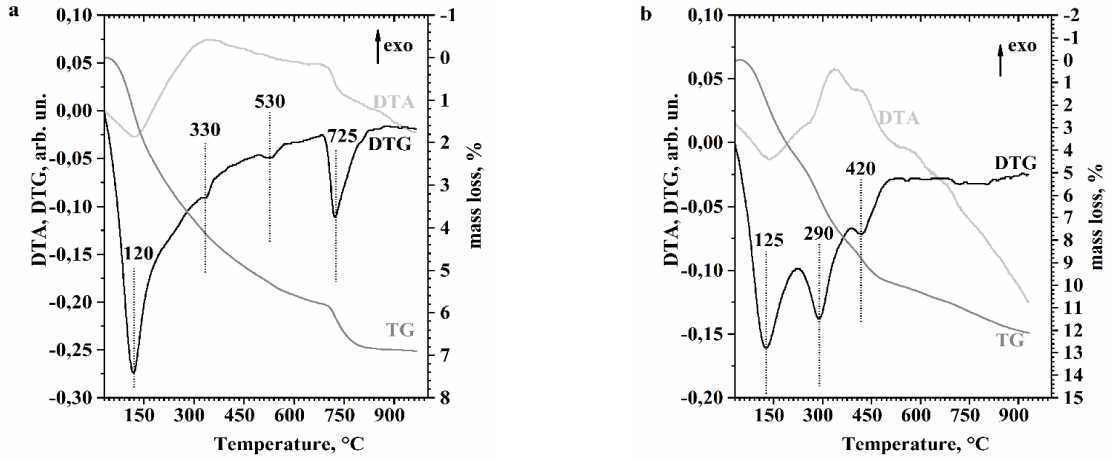

Fig. 6. TG/DTG/DTA curves of HA (*a*) and pHA:Tb/Citr (*b*) samples

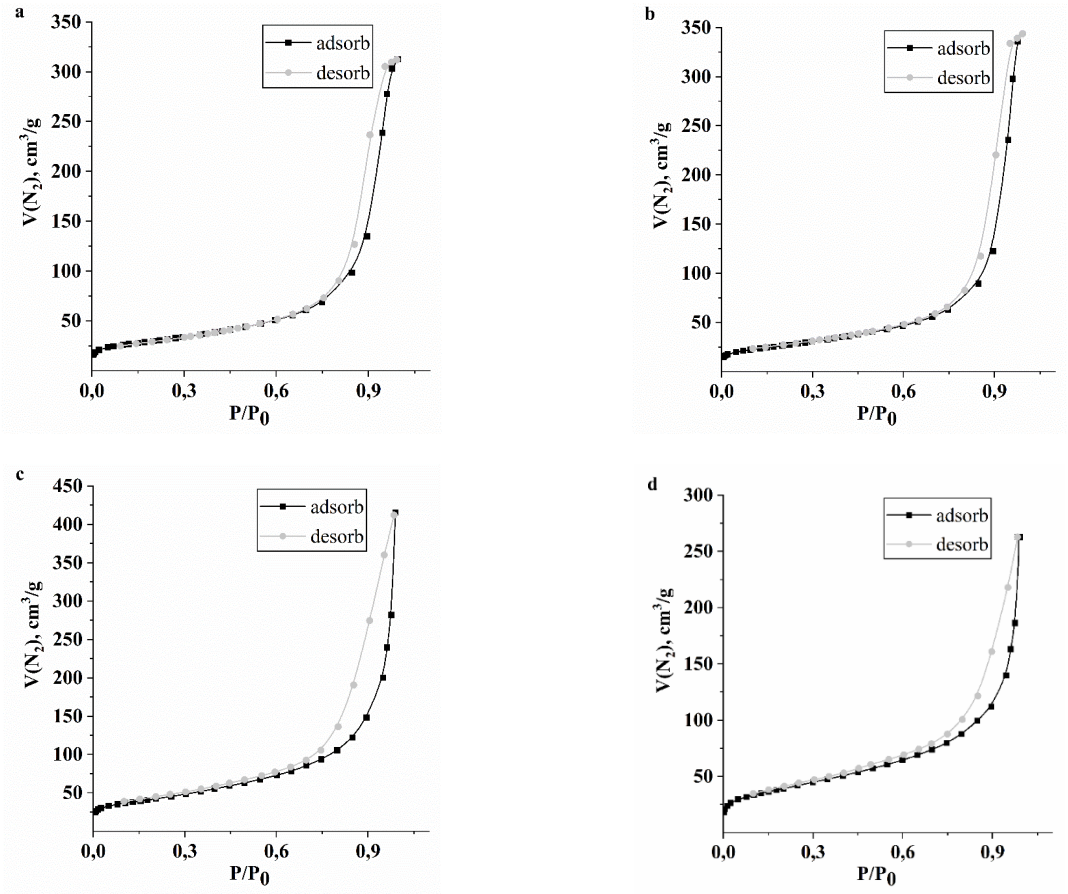

Fig. 7. Isotherms of low-temperature nitrogen adsorption-desorption for HA (*a*), HA/Citr (*b*), HA:Tb (*c*), HA:Tb/Citr (*d*) samples. $V(N_2)$ – the volume of adsorbed nitrogen, P_0 – the initial nitrogen pressure, P – the nitrogen pressure after adsorption

Table 5. Results of the study of weight loss demonstrated by TGA for HA and pHA:Tb/Citr samples

Sample	Mass loss, %				Residue, %
	Total loss	25-200 °C	200-600 °C	600-1000 °C	
HA	6.9	2.76	2.83	1.3	93.1
pHA:Tb/Citr	12.2	3.84	6.38	1.98	87.8

The textural properties and isotherm characteristics of HA:Tb clearly demonstrate significant changes. The material exhibits a more developed mesoporous network, as evidenced by the increase in total pore volume to 0.64 cm^3/g. The average pore diameter decreased to 172.3 nm compared to undoped HA.

HA:Tb displays a type IV isotherm that is typical for mesoporous materials with an H2 hysteresis loop indicating the ink-bottle-shaped pores [67–69].

In contrast, pHA:Tb/Citr possesses a slightly smaller total pore volume compared to HA:Tb, measuring at 0.60 cm^3/g. However, it has the smallest average pore diameter among all samples, namely 115.4 nm. This indicates that citrate ions significantly influenced the microporosity of the material (Fig. 8) that is consistent with the data obtained by the BJH method. The H2 hysteresis loop observed in the N_2 adsorption-desorption isotherm (Fig. 7) supports this observation as well.

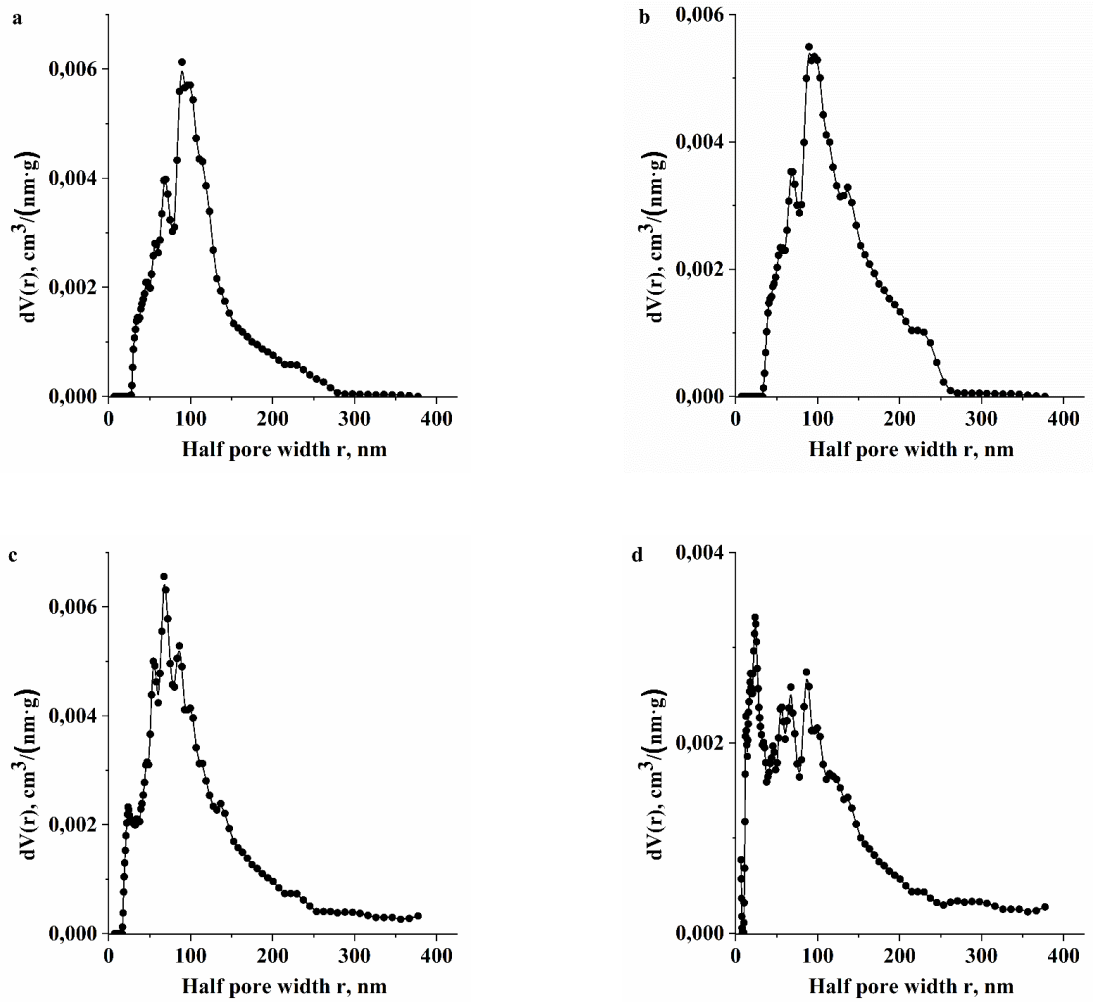

Fig. 8. Pore size distribution curves for HA (*a*), HA/Citr (*b*), HA:Tb (*c*), and HA:Tb/Citr (*d*) samples. *V* – pore volume, *r* – pore radius

Table 6. Results of low-temperature nitrogen adsorption-desorption for HA, HA/Citr, HA:Tb, HA:Tb/Citr samples

Sample	Surface area, m^2/g	Pore volume, cm^3/g	Micropore volume, cm^3/g	Mean pore size, nm
HA	104.8	0.48	0.039	184.5
HA/Citr	94.4	0.53	0.035	225.2
HA:Tb	149.2	0.64	0.056	172.3
HA:Tb/Citr	140.7	0.41	0.048	115.4

CONCLUSIONS

In accordance with the aim of the work, nanostructured terbium-doped hydroxyapatite samples with modified surface were synthesized and characterized. Among the various synthesized samples, those prepared using the Ca^{2+} and Tb^{3+} ions co-precipitation method in the presence of trisodium citrate dihydrate modifier (pHA:Tb/Citr) exhibited superior X-ray-induced luminescence and colloidal characteristics.

The surface modification with citrate groups resulted in a stoichiometric ratio (Ca+Tb)/P close to natural hydroxyapatite. The high ζ-potential value (-33.9 mV) indicated that the sample possessed excellent colloidal stability, along with potential for high adsorption capability and enhanced biocompatibility compared to other samples. The nanoparticles of pHA:Tb/Citr are needle-shaped with an average size of 121.07±35.47 nm. The XRD analysis confirmed the preservation of the hydroxyapatite crystal structure regardless of tolerance and surface modification. The presence of surface carboxyl groups was revealed by the FTIR analysis. At the same time, the TG/DTG/DTA analysis showed the presence of citrate molecules on the surface, which contain carboxyl groups in their structure. The FT-NIR study showed an increase in surface activity against HA and HA:Tb due to surface groups. The BET surface area analysis showed that the doping with terbium significantly changes the textural properties, increasing the surface area by almost 50 % relative to HA by increasing the micropore volume and decreasing the average pore size.

The results of the study show that a nanophosphor with the most optimal properties for biomedical applications, such as low toxicity and the possibility of further surface functionalization for adsorption saturation with molecules of medical interest, was obtained.

Синтез та характеризація нанорозмірного люмінесцентного гідроксиапатиту, допованого тербієм

О.Д. Щеглов, А.П. Кусяк, Р.М. Кравчук, Я.М. Шуба, А.Л. Петрановська, П.П. Горбик

Інститут хімії поверхні ім. О.О. Чуйка Національної академії наук України
вул. Генерала Наумова, 17, Київ, 03164, Україна, ol.shchehlov@gmail.com
Інститут фізики Національної академії наук України
просп. Науки, 46, Київ, 03028, Україна
Інститут фізіології ім. О.О. Богомольця Національної академії наук України
вул. Академіка Богомольця, 4, Київ, 01601, Україна

Метою роботи є синтез нового наноструктурованого біосумісного матеріалу з високою здатністю до рентгеноіндукованої люмінесценції. Було синтезувано допований тербієм гідроксиапатит, відомий своєю біосумісністю та нетоксичністю, двома способами: 1) осадженням іонів Ca^{2+} та Tb^{3+} розчином $(NH_4)_2HPO_4$ у присутності різних біосумісних модифікаторів (CTAB, PEG-2000, тринатрію цитрату дигідрат); 2) катіонним заміщенням гідроксиапатиту в присутності тих самих модифікаторів при pH 4 і pH 6. Стехіометричне співвідношення (Ca+Tb)/P у вихідних розчинах підтримували на рівні біологічного гідроксиапатиту).

В результаті досліджень DLS, ELS та аналізу рентгеноіндукованої люмінесценції було встановлено, що найкращі ключові властивості, такі як ζ-потенціал і рентгеноіндукована люмінесценція, має зразок

допованого 5 % (мол.) гідроксиапатиту, синтезованого методом співосадження в присутності тринатрію цитрату дигідрату. В результаті подальших досліджень методами TEM, FTIR, FT-NIR, TG/DTG/DTA, XRD, низькотемпературної адсорбції-десорбції азоту та ICP-AES було встановлено, що зразок має модифіковану цитратними групами поверхню, що зумовлює його високу колоїдну стабільність та може надавати високий адсорбційний потенціал. Значення співвідношення (Ca+Tb)/P становить 2.21 (мас.), що є близьким до значення біологічного гідроксиапатиту. Нанокомпозит характеризується високою рентгеноіндукованою люмінесценцією і може бути перспективним для адсорбційної іммобілізації біологічно активних сполук.

Результати дослідження свідчать про те, що знайдено оптимальні умови синтезу нанолюмінофорів, які є потенційними кандидатами для біомедичного застосування, враховуючи люмінесцентні властивості, низьку токсичність та можливість подальшої функціоналізації поверхні для адсорбційного насичення молекулами, що становлять медичний інтерес.

***Ключові слова**: наночастинки, нанокомпозити, люмінесценція, лантаніди, гідроксиапатит, тербій*

REFERENCES

1. Srinivasan M., Rajabi M., Mousa S. Multifunctional Nanomaterials and Their Applications in Drug Delivery and Cancer Therapy. *Nanomaterials*. 2015. **5**(4): 1690.
2. Reiss P., Protière M., Li L. Core/Shell Semiconductor Nanocrystals. *Small*. 2009. **5**(2): 154.
3. Lin M., Zhao Y., Wang S., Liu M., Duan Z., Chen Y., Li F., Xu F., Lu T. Recent Advances in Synthesis and Surface Modification of Lanthanide-doped Upconversion Nanoparticles for Biomedical Applications. *Biotechnol. Adv.*, 2012. **30**(6): 1551.
4. Zheng B., Fan J., Chen B., Qin X., Wang J., Wang F., Deng R., Liu X. Rare-Earth Doping in Nanostructured Inorganic Materials. *Chem. Rev*. 2022. **122**(6): 5519.
5. Kang X., Huang S., Yang P., Ma P., Yang D., Lin J. Preparation of Luminescent and Mesoporous Eu^{3+}/Tb^{3+} Doped Calcium Silicate Microspheres as Drug Carriers via a Template Route. *Dalton Trans*. 2011. **40**(9): 1873.
6. Wu Y., Wang Y., He D., Fu M., Chen Z., Li Y. Spherical $Zn_2SiO_4:Eu^{3+}@SiO_2$ Phosphor Particles in Core–shell Structure: Synthesis and Characterization. *J. Lumin.* 2010. **130**(10): 1768.
7. Zhong S.-L., Lu Y., Gao M.-R., Liu S.-J., Peng J., Zhang L.-C., Yu S.-H. Monodisperse Mesocrystals of YF_3 and Ce^{3+}/Ln^{3+} (Ln = Tb, Eu) Co-Activated YF_3: Shape Control Synthesis, Luminescent Properties, and Biocompatibility. *Chem. Eur. J.* 2012. **18**(17): 5222.
8. Yang M., You H., Liu K., Zheng Y., Guo N., Zhang H. Low-Temperature Coprecipitation Synthesis and Luminescent Properties of $LaPO_4:Ln^{3+}$ (Ln^{3+} = Ce^{3+}, Tb^{3+}) Nanowires and $LaPO_4:Ce^{3+}$, $Tb^{3+}/LaPO_4$ Core/Shell Nanowires. *Inorg. Chem*. 2010. **49**(11): 4996.
9. Liu H., Chen F., Xi P., Chen B., Huang L., Cheng J., Shao C., Wang J., Bai D., Zeng Z. Biocompatible Fluorescent Hydroxyapatite: Synthesis and Live Cell Imaging Applications. *J. Phys. Chem. C*. 2011. **115**(38): 18538.
10. Krishnapriya T.K., Deepti A., Chakrapani P.S., Asha A.S., Jayaraj M.K. Biocompatible, Europium-Doped Fluorapatite Nanoparticles as a Wide-Range pH Sensor. *J. Fluoresc.* 2023. **34**: 2543.
11. Lara-Ochoa S., Ortega-Lara W., Guerrero-Beltrán C.E. Hydroxyapatite Nanoparticles in Drug Delivery: Physicochemistry and Applications. *Pharmaceutics*. 2021. **13**(10): 1642.
12. Uskokovic V., Desai T.A. Phase Composition Control of Calcium Phosphate Nanoparticles for Tunable Drug Delivery Kinetics and Treatment of Osteomyelitis. I. Preparation and drug release. *J. Biomed. Mater. Res. A.* 2013. **101**(5): 1416.
13. Matsumoto T., Okazaki M., Inoue M., Yamaguchi S., Kusunose T., Toyonaga T., Hamada Y., Takahashi J. Hydroxyapatite Particles as a Controlled Release Carrier of Protein. *Biomaterials*. 2004. **25**(17): 3807.
14. Zhang S., Ma X., Sha D., Qian J., Yuan Y., Liu C. A Novel Strategy for Tumor Therapy: Targeted, PAA-Functionalized Nano-hydroxyapatite Nanomedicine. *J. Mater. Chem. B*. 2020. **8**(41): 9589.
15. Venkatasubbu G.D., Ramasamy S., Avadhani G.S., Ramakrishnan V., Kumar J. Surface Modification and Paclitaxel Drug Delivery of Folic Acid Modified Polyethylene Glycol Functionalized Hydroxyapatite Nanoparticles. *Powder Technol.* 2013. **235**: 437.
16. Gu M., Li W., Jiang L., Li X. Recent Progress of Rare Earth Doped Hydroxyapatite Nanoparticles: Luminescence Properties, Synthesis and Biomedical Applications. *Acta Biomater*. 2022. **148**: 22.
17. Neacsu I.A., Stoica A.E., Vasile B.S., Andronescu E. Luminescent Hydroxyapatite Doped with Rare Earth Elements for Biomedical Applications. *Nanomaterials*. 2019. **9**(2): 239.

18. De Lama-Odría M.d.C., Valle L.J.d., Puiggalí J. Lanthanides-Substituted Hydroxyapatite for Biomedical Applications. *Int. J. Mol. Sci*. 2023. **24**(4): 3446.
19. Šupová M. Substituted Hydroxyapatites for Biomedical Applications: a Review. *Ceram. Int*. 2015. **41**(8): 9203.
20. Kusyak A., Petranovska A., Oranska O., Turanska S., Shuba Ya., Kravchuk D., Kravchyk L., Sotkis G., Nazarenko V., Kravchuk R., Dubok V., Bur'yanov O., Chornyi V., Sobolevs'kyy Yu., Gorbyk P. *Synthesis and Properties of Nanodispersed Luminescent Structures Based on Lanthanum Fluoride and Phosphate for Optopharmacology and Photodynamic Therapy of Tumor Diseases Localized in Cranial Organs and Bone Tissues.* Chapter 3. (New York: Nova Science Publishers Inc., 2023).
21. Zilm M.E., Chen L., Sharma V., McDannald A., Jain M., Ramprasad R., Wei M. Hydroxyapatite Substituted by Transition Metals: Experiment and Theory. *Phys. Chem. Chem. Phys*. 2016. **18**(24): 16457.
22. Tite T., Popa A.-C., Balescu L.M., Bogdan I.M., Pasuk I., Ferreira J.M.F., Stan G.E. Cationic Substitutions in Hydroxyapatite: Current Status of the Derived Biofunctional Effects and Their In Vitro Interrogation Methods. *Materials*. 2018. **11**(11): 2081.
23. Chen M.-H., Yoshioka T., Ikoma T., Hanagata N., Lin F.-H., Tanaka J. Photoluminescence and Doping Mechanism of Theranostic Eu^{3+}/Fe^{3+} Dual-doped Hydroxyapatite Nanoparticles. *Sci. Technol. Adv. Mater*. 2014. **15**(5): 055005.
24. Alshemary A.Z., Akram M., Goh Y.-F., Abdul Kadir M.R., Abdolahi A., Hussain R. Structural Characterization, Optical Properties and In Vitro Bioactivity of Mesoporous Erbium-doped Hydroxyapatite. *J. Alloys Compd*. 2015. **645**: 478.
25. Ahmed L.O., Bulut N., Bañares L., Kaygili O., Kebiroglu M., Ates T., Koytepe S., Ates B. Exploring the Electronic Band Structure, Spectroscopic Signatures, and Structural Properties of Er^{3+}-based Hydroxyapatites Co-doped with Ce^{3+} Ions. *Inorg. Chem. Commun*. 2023. **155**(37): 111067.
26. Wei Y., He Y., Li X., Chen H., Deng X. Cellular Uptake and Delivery-Dependent Effects of Tb^{3+}-Doped Hydroxyapatite Nanorods. *Molecules*. 2017. **22**(7): 1043.
27. Yin H., Li Y., Bai J., Ma M., Liu J. Effect of Calcinations Temperature on the Luminescence Intensity and Fluorescent Lifetime of Tb^{3+}-doped Hydroxyapatite (Tb-HA) Nanocrystallines. *J. Materiomics*. 2017. **3**(2): 144.
28. Ghosh R., Sarkar R., Paul S. Development of Machinable Hydroxyapatite-Lanthanum Phosphate Composite for Biomedical Applications. *Mater. Design*. 2016. **106**: 161.
29. Venkatasubbu G.D., Ramasamy S., Avadhani G.S., Ramakrishnan V., Kumar J. Surface Modification and Paclitaxel Drug Delivery of Folic Acid Modified Polyethylene Glycol Functionalized Hydroxyapatite Nanoparticles. *Powder Technol.* 2013. **235**: 437.
30. Cawthray J.F., Creagh A.L., Haynes C.A., Orvig C. Ion Exchange in Hydroxyapatite with Lanthanides. *Inorg. Chem*. 2015. **54**(4): 1440.
31. Li L., Liu Y., Tao J., Zhang M., Pan H., Xu X., Tang R. Surface Modification of Hydroxyapatite Nanocrystallite by a Small Amount of Terbium Provides a Biocompatible Fluorescent Probe. *J. Phys. Chem. C*. 2008. **112**(32): 12219.
32. Huang S., Zhu J., Zhou K. Synthesis and Luminescence Properties of Tb^{3+}-Doped Hydroxyapatites. *Adv. Mater. Res*. 2012. **399–401**: 1582.
33. Yin H., Li Y., Bai J., Ma M., Liu J. Effect of Calcinations Temperature on the Luminescence Intensity and Fluorescent Lifetime of Tb^{3+}-doped Hydroxyapatite (Tb-HA) Nanocrystallines. *J. Materiomics*. 2017. **3**(2): 144.
34. Ou X., Qin X., Huang B., Zan J., Wu Q., Hong Z., Xie L., Bian H., Yi Z., Chen X., Wu Y., Song X., Li J., Chen Q., Yang H., Liu X. High-resolution X-ray Luminescence Extension Imaging. *Nature*. 2021. **590**(7846): 410.
35. Xu Z., Li Y., Liu Z., Wang D. UV and X-ray Excited Luminescence of Tb^{3+}-doped $ZnGa_2O_4$ Phosphors. *J. Alloys Compd.* 2005. **391**(1–2): 202.
36. Ciobanu C.S., Iconaru S.L., Massuyeau F., Constantin L.V., Costescu A., Predoi D. Synthesis, Structure, and Luminescent Properties of Europium-Doped Hydroxyapatite Nanocrystalline Powders. *J. Nanomater*. 2012. **212**: 942801.
37. Wei Y., He Y., Li X., Chen H., Deng X. Cellular Uptake and Delivery-Dependent Effects of Tb^{3+}-Doped Hydroxyapatite Nanorods. *Molecules.* 2017. **22**(7): 1043.
38. Paduraru A.V., Oprea O., Musuc A.M., Vasile B.S., Iordache F., Andronescu E. Influence of Terbium Ions and Their Concentration on the Photoluminescence Properties of Hydroxyapatite for Biomedical Applications. *Nanomaterials*. 2021. **11**(9): 2442.
39. Gómez-Morales J., Fernández-Penas R., Acebedo-Martínez F.J., Romero-Castillo I., Verdugo-Escamilla C., Choquesillo-Lazarte D., Esposti L.D., Jiménez-Martínez Y., Fernández-Sánchez J.F., Iafisco M., Boulaiz H. Luminescent Citrate-Functionalized Terbium-Substituted Carbonated Apatite Nanomaterials: Structural Aspects, Sensitized Luminescence, Cytocompatibility, and Cell Uptake Imaging. *Nanomaterials.* 2022. **12**(8): 1257.

40. Daryan S. H., Khavandi A., Javadpour, J. Surface Engineered Hollow Hydroxyapatite Microspheres: Hydrothermal Synthesis and Growth Mechanisms. *Solid State Sci*. 2020. **106**: 106301.
41. Shang H.-B., Chen F., Wu J., Qi C., Lu B.-Q., Chen X., Zhu Y.-J. Multifunctional Biodegradable Terbium-doped Calcium Phosphate Nanoparticles: Facile Preparation, pH-sensitive Drug Release and In Vitro Bioimaging. *RSC Adv.*, 2014. **4**(95): 53122.
42. Simon A.T., Dutta D., Chattopadhyay A., Ghosh S. S. Copper Nanocluster-Doped Luminescent Hydroxyapatite Nanoparticles for Antibacterial and Antibiofilm Applications. *ACS Omega*. 2019. **4**(3): 4697.
43. De Lama-Odría M.d.C., Valle L.J.d., Puiggalí J. Lanthanides-Substituted Hydroxyapatite for Biomedical Applications. *Int. J. Mol. Sci*. 2023. **24**(4): 3446.
44. Gu M., Li W., Jiang L., Li X. Recent Progress of Rare Earth Doped Hydroxyapatite Nanoparticles: Luminescence Properties, Synthesis and Biomedical Applications. *Acta Biomater*. 2022. **148**: 22.
45. Ignjatović N.L., Mančić L., Vuković M., Stojanović Z., Nikolić M.G., Škapin S., Jovanović S., Veselinović L., Uskoković V., Lazić S., Marković S., Lazarević M.M., Uskoković D.P. Rare-earth (Gd^{3+}, Yb^{3+}/Tm^{3+}, Eu^{3+}) Co-doped Hydroxyapatite as Magnetic, Up-conversion and Down-conversion Materials for Multimodal Imaging. *Sci. Rep*. 2019. **9**(1): 16305.
46. Kusyak A.P., Petranovska A.L., Turanska S.P., Oranska O.I., Shuba Ya.M., Kravchuk D.I., Kravchuk L.I., Nazarenko V.G., Kravchuk R.M., Dubok V.A., Chornyi V.S., Bur'yanov O.A., Sobolevs'kyy Yu.L., Gorbyk P.P. Synthesis, Properties and Application Possibilities of X-ray Luminescent Nanocrystalline Lanthanum Phosphate. *Chemistry, Physics and Technology of Surface*. 2022. **13**(4): 425.
47. Kusyak A.P., Petranovska A.L., Oranska O.I., Turanska S.P., Shuba Ya.M., Kravchuk D.I., Kravchuk L.I., Sotkis G.V., Nazarenko V.G., Kravchuk R.M., Dubok V.A., Bur'yanov O.A., Chornyi V.S., Sobolevs'kyy Yu.L., Gorbyk P.P. X-ray Luminescent Nanostructures Based on Lanthanum Fluoride and Phosphate for Optopharmacology and Photodynamic Therapy of Tumor Diseases. *Poverhnia*. 2023. **15(30)**: 268. [in Ukrainian].
48. Kusyak A., Petranovska A., Shchehlov O., Kravchuk R., Shuba Ya., Gorbyk P. X-ray Luminescent Nanocomposite LaF_3:Tb/Citr@$[Ru(bpy)_2(nic)_2]^{2+}$ as a Model Targeted Delivery System for Photopharmacology and Photodynamic Therapy. *Hybrid Advances*. 2024. **5**: 100154.
49. Lu Y.H., Xiao X.F., Zheng X. Wu S.S., Liu R.F. Hydrothermal Synthesis and Characterization of Tb^{3+} Doped Hydroxyapatite. *Adv. Mater. Res*. 2012. **391**: 709.
50. Bhattacharjee S. DLS and Zeta Potential – Why They Are and What They Are Not? *J. Control. Release.* 2016. **235**(2016): 337.
51. Han Y., Wang X., Dai H., Li S. Nanosize and Surface Charge Effects of Hydroxyapatite Nanoparticles on Red Blood Cell Suspensions. *ACS Appl. Mater. Interfaces.* 2012. **4**(9): 4616.
52. Chen L., Mccrate J.M., Lee J.C-M., Li H. The Role of Surface Charge on the Uptake and Biocompatibility of Hydroxyapatite Nanoparticles with Osteoblast Cells. *Nanotechnology.* 2011. **22**(10) 105708.
53. Turon P., Del Valle L.J., Alemán C., Puiggali J. Biodegradable and Biocompatible Systems Based on Hydroxyapatite Nanoparticles. *Appl. Sci.* 2017. **7**(1): 60.
54. Wang C., Jeong K.-J., Kim J., Kang S.W., Kang J., Han I.H., Lee I.-W., Oh S.-J., Lee J. Emission-tunable Probes Using Terbium(III)-doped Self-activated Luminescent Hydroxyapatite for In Vitro. *J. Colloid Interface Sci.* 2021. **581**(A): 21.
55. Yang C., Yang P., Wang W., Zhang M., Lin J. Solvothermal Synthesis and Characterization of Ln (Eu^{3+}, Tb^{3+}) Doped Hydroxyapatite. *J. Colloid Interface Sci.* 2008. **328**(1): 203.
56. Venkatasubbu G.D., Ramasamy S., Ramakrishnan V., Kumar J. Nanocrystalline Hydroxyapatite and Zinc-doped Hydroxyapatite as Carrier Material for Controlled Delivery of Ciprofloxacin. *3 Biotech*. 2011. **1**(3): 173.
57. Koort J.K., Mäkinen T.J., Suokas E., Veiranto M., Jalava J., Törmälä P., Aro H.T. Sustained Release of Ciprofloxacin from an Osteoconductive Poly(DL)-lactide Implant. *Acta Orthop*. 2008. **79**(2): 295.
58. Chaussemier M., Pourmohtasham E., Gelus D., Pécoul N., Perrot H., Lédion J., Cheap-Charpentier H., Horner O. State of Art of Natural Inhibitors of Calcium Carbonate Scaling. A Review Article. *Desalination*. 2015. **356**: 47.
59. Li J., Liu Y., Gao Y., Zhong L., Zou Q., Lai X. Preparation and Properties of Calcium Citrate Nanosheets for Bone Graft Substitute. *Bioengineered*. 2016. **7**(5): 376.
60. Kolmas J., Marek D., Kolodziejski W. Near-Infrared (NIR) Spectroscopy of Synthetic Hydroxyapatites and Human Dental Tissues. *Appl. Spectrosc*. 2015. **69**(8): 902.
61. Grabska J., Ishigaki M., Beć K.B., Wojcik M.J., Ozaki Y. Correlations between Structure and Near-Infrared Spectra of Saturated and Unsaturated Carboxylic Acids. Insight From Anharmonic Density Functional Theory Calculations. *J. Phys. Chem. A.* 2017. **121**(18): 3437.
62. Barbooti M.M., Al-Sammerrai D.A. Thermal Decomposition of Citric Acid. *Termochim. Acta*. 1986. **98**: 119.
63. Mansour S.A.A. Thermal Decomposition of Calcium Citrate Tetrahydrate. *Thermochim. Acta.* 1994. **233**: 243.

64. Sing K.S.W. Reporting Physisorption Data for Gas/solid Systems with Special Reference to the Determination of Surface Area and Aorosity (Recommendations 1984). *Pure Appl. Chem.* 1985. **57**(4): 603.
65. Xia X., Chen J., Shen J., Huang D., Duan P., Zou G. Synthesis of Hollow Structural Hydroxyapatite with Different Morphologies Using Calcium Carbonate as Hard Template. *Adv. Powder Technol*. 2018. **29**(7): 1562.
66. Rhati H., Laghzizil A., Saoiabi A., El Asri S., Lahlil K., Gacoin T. Surface Properties of Porous Hydroxyapatite Derived from Natural Phosphate. *Mater. Chem. Phys*. 2012. **136**(2–3): 1022.
67. Zhang Y., Shao D., Yan J., Jia X., Li Y., Yu P., Zhang T. The Pore Size Distribution and its Relationship with Shale Gas Capacity in Organic-rich Mudstone of Wufeng-Longmaxi Formations, Sichuan Basin, China. *J. Nat. Gas Geosci*. 2016. **1**(3): 213.
68. Chen Z., Liu Y., Mao L., Gong L., Sun W., Feng L. Effect of Cation Doping on the Structure of Hydroxyapatite and the Mechanism of Defluoridation. *Ceram. Int.* 2018. **44**(6): 6002.
69. Thommes M., Kaneko K., Neimark A.V., Olivier J.P., Rodriguez-Reinoso F., Rouquerol J., Sing K.S.W. Physisorption of Gases, with Special Reference to the Evaluation of Surface Area and Pore Size Distribution (IUPAC Technical Report). *Pure Appl. Chem.* 2015. **87**(9–10): 1051.

Received 31.07.2024, accepted 05.03.2025